Journal of Laser Applications

RESEARCH ARTICLE | OCTOBER 02 2023

On the limitations of small cubes as test coupons for process parameter optimization in laser powder bed fusion of metals

Special Collection: Proceedings of the International Congress of Applications of Lasers & Electro-Optics (ICALEO 2023)

Gunther Mohr ; Simon J. Altenburg ; Kai Hilgenberg

Check for updates

J. Laser Appl. 35, 042029 (2023)
https://doi.org/10.2351/7.0001080

View Online
Export Citation
CrossMark

Articles You May Be Interested In

Method for casting epoxy tensile coupons

Rev Sci Instrum (August 2008)

UNESCO's Book Coupons

Physics Today (March 1951)

Stresses in painted steel coupons from stone impact

AIP Conference Proceedings (July 1994)

25 October 2023 08:06:05

ALIA THE LASER INSTITUTE
Journal of Laser Applications
Learn More
RAPID TIME TO ACCEPTANCE
COMMUNITY DRIVEN
EXPANSIVE COVERAGE
PRESTIGIOUS EDITORIAL BOARD
EXTENSIVE MARKETING

ALIA THE LASER INSTITUTE

Journal of Laser Applications ARTICLE pubs.aip.org/lia/jla

On the limitations of small cubes as test coupons for process parameter optimization in laser powder bed fusion of metals

Cite as: J. Laser Appl. 35, 042029 (2023); doi: 10.2351/7.0001080
Submitted: 16 June 2023 · Accepted: 14 September 2023 ·
Published Online: 2 October 2023

View Online Export Citation CrossMark

Gunther Mohr,[a] Simon J. Altenburg, and Kai Hilgenberg

AFFILIATIONS

Bundesanstalt für Materialforschung und -prüfung (BAM), Unter den Eichen 87, Berlin 12205, Germany

Note: Paper published as part of the special topic on Proceedings of the International Congress of Applications of Lasers & Electro-Optics 2023.

[a]**Electronic mail:** gunther.mohr@bam.de

ABSTRACT

The capability to produce complexly and individually shaped metallic parts is one of the main advantages of the laser powder bed fusion process. Development of material and machine specific process parameters is commonly based on the results acquired from small cubic test coupons of ~10 mm edge length. Such cubes are usually used to conduct the optimization of process parameters to produce dense materials. The parameters are then taken as the basis for the manufacturing of real part geometries. However, complex geometries go along with complex thermal histories during the manufacturing process, which can significantly differ from thermal conditions prevalent during the production of simply shaped test coupons. This may lead to unexpected and unpredicted local inhomogeneities of the microstructure and defect distribution in the final part, and it is a root cause of reservations against the use of additive manufacturing for the production of safety relevant parts. In this study, the influence of changing thermal conditions on the resulting melt pool depth of 316L stainless steel specimens is demonstrated. A variation in thermographically measured intrinsic preheating temperatures was triggered by the alteration of interlayer times and a variation in cross-sectional areas of specimens for three distinct sets of process parameters. Correlations between the preheating temperature, the melt pool depth, and occurring defects were analyzed. The limited expressiveness of the results of small density cubes is revealed throughout the systematic investigation. Finally, a clear recommendation to consider thermal conditions in future process parameter optimizations is given.

25 October 2023 08:06:05

Key words: additive manufacturing, heat accumulation, thermal history, thermography, *in situ* monitoring, selective laser melting, laser beam melting, representative specimens

© *2023 Author(s). All article content, except where otherwise noted, is licensed under a Creative Commons Attribution (CC BY) license (http://creativecommons.org/licenses/by/4.0/).* https://doi.org/10.2351/7.0001080

INTRODUCTION

Laser powder bed fusion (PBF-LB/M) has the biggest market share in the field of metallic additive manufacturing (AM) technologies.[1] Its outstanding capability to produce complexly and individually shaped metallic parts out of a loose powder bed accounts for its competitive position when it comes to the manufacturing of small lot sizes despite high costs of the raw material and processing. In addition to economic cost restrictions, there are still limitations in the field of safety relevant parts, as local inhomogeneities of the microstructure and the distribution of defects might unexpectedly and unpredictably occur within a component. This has been identified as a major challenge for the use of PBF-LB/M.[2–4]

One of the materials that have been studied very intensely in the context of PBF-LB/M processing is austenitic stainless steel 316L. Figure 1 summarizes several values of ultimate tensile strength (UTS) of 316L manufactured by PBF-LB/M derived from the literature.[12] The figure displays the minimum and maximum published UTS of each individual source. To ensure a valid comparison, the diagram focuses on values determined from horizontally built, nonheat-treated specimens. The presented UTS values range from 178 MPa as the worst minimum value to 755 MPa as

© Author(s) 2023

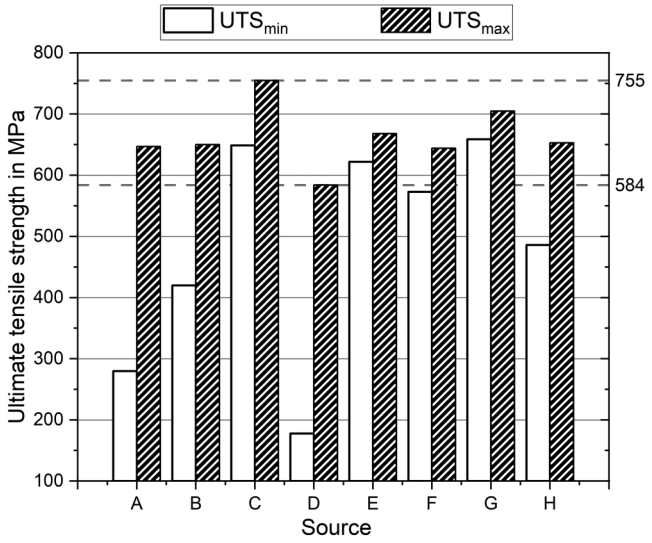

FIG. 1. Comparison of UTS values of horizontally built 316L specimens. The minimum and maximum UTS of each source is displayed. The values were taken from literature (A: Ref. 5; B: Ref. 6; C: Ref. 7; D: Ref. 8; E: Ref. 9; F: Ref. 10; G: Ref. 11; H: Ref. 2). Sources G and H are referred to as review publications, which incorporate already different other studies.

the best maximum value in the respective studies. The minimum values might distort the comparison as they might be derived from specimens built by inappropriate processing parameters as part of a broad parameter variation study. However, even when considering the maximum values only, deviations of up to 23% are noticeable, which should not be tolerable in terms of a stable process result for the same material used. Röttger *et al.*[10] conducted a round robin test using four different PBF-LB/M machines and their individual best practice parameter sets for 316L. The results are depicted in Fig. 1, source F. They found a spreading of 11% in UTS for the horizontally built specimens. This implies that the use of a particular PBF-LB/M system can be already understood as one additional influencing factor affecting further factors. The particular system used for specimen production and its respective settings are not reported in every case in the literature. Other missing data are precise information about the specimen geometry in the as-built state in some cases. Much more often, information about the number of parts per build plate or the resulting ratio of area exploitation (RAE) as well as the resulting interlayer time (ILT) is missing. To date, these factors are not considered regularly in test programs and are, therefore, often neglected. The given example of significant deviations of published mechanical properties underlines the importance of two exigent issues in the field of additive manufacturing: provision of reliable material reference data and comprehensive documentation of processing conditions. To meet the necessary requirements for this, the starting point should already be set at the very beginning of a material qualification process, which is usually the batch production of small cubes as test coupons for process parameter optimization. Hence, the conditions of a typical material qualification process must be reviewed.

The choice of the right set of processing parameters is very important for the manufacturing result. Consequently, the identification of a suitable process window by parameter optimization is mandatory prior to any manufacturing. A strong focus of any process parameter window identification is primarily set on the production of specimens free of defects, such as porosity, cracks, dimensional accuracy, and others.[13] The first goal in PBF-LB/M process optimization is usually to create parts with a high density (>99.5%).[11] The usual process parameter optimization consists of two steps: defect minimization and second mechanical and chemical testing.[13] The defect minimization is typically conducted via a batch production of a high amount of small cubic samples with varying process parameters. The small samples are then taken for density analysis. The dimensions of these laboratory specimens do usually not exceed a built height of 15 mm. A typical number of specimens per built ranges between 24 and 50, which may differ due to different build plate sizes. For instance, Bang *et al.*[6] studied the effect of processing parameters on the density of 316L cubes of the dimension of $10 \times 10 \times 10\,\mathrm{mm}^3$, building 36 of these cubes in one build process. Carrozza *et al.*[14] built 36 cubes of the dimension of $15 \times 15 \times 15\,\mathrm{mm}^3$ from Ti–6Al–2Sn–4Zr–6Mo in one build process to determine a suitable processing window for low porosity. Wang *et al.*[15] used cuboids of the dimensions of $10 \times 10 \times 8\,\mathrm{mm}^3$, building 24 of them from Ti–6Al–4V within one build process. The outcome of these studies is one or a few sets of processing parameters for further analysis and eventually final part production. Such a process parameter optimization is mainly driven by a variation in the main energy input related influencing factors. Figure 1 shows the comparison of UTS values of horizontally built 316L specimens. The minimum and maximum UTS of each source is displayed. The values were taken from the literature (A: Ref. 5; B: Ref. 6; C: Ref. 7; D: Ref. 8; E: Ref. 9; F: Ref. 10; G: Ref. 11; H: Ref. 2). Sources G and H are referred to review publications, which incorporate already different other studies.

Figure 2 schematically illustrates the usual process parameters, which are varied in the context of the laser exposition of a powder layer.[12] The drawn melt pool shape depicts the typical keyhole morphology as the deep penetration mode welding or transition mode welding is reported over a broad range of parameter combinations for 316L stainless steel,[16] which was also used in the experimental part of this study.

In many cases, a selection of these processing parameters is summarized into different auxiliary values to describe the energy input: one-dimensional energy input per unit length (laser power divided by scanning velocity),[17,18] two-dimensional energy input per unit area (hatch distance or spot size added to the denominator),[18] and three-dimensional volumetric energy density (VED), as stated in the following equation:

$$VED = \frac{P_L}{v_S\, h_S\, t}. \tag{1}$$

The level of VED can affect the melt pool size and also the welding regime in the way that an increasing VED leads not only to a growing melt pool but potentially also to a transition from conduction mode welding to deep penetration or keyhole mode

25 October 2023 08:06:05

© Author(s) 2023

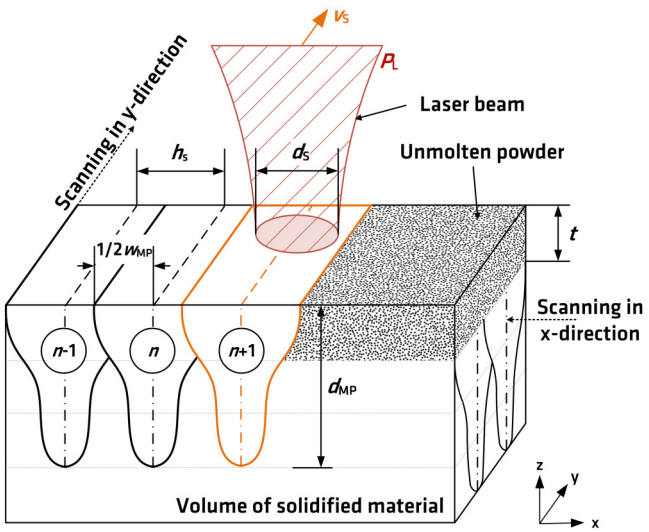

FIG. 2. Schematic of the melting process highlighting the main processing parameters (laser power P_L, scanning velocity v_S, hatch distance h_S, laser spot size d_S, layer thickness t) and melt pool dimensions (depth d_{MP} and width w_{MP}). A x-y-scanning strategy is displayed with a 90° rotation of the scanning pattern after every layer.

welding.[19,20] In addition, the risk of discontinuous melt tracks and balling phenomena with decreasing VED were shown[19] as well as the occurrence of lack of fusion defects at a rather low VED level.[13] An increase in the amount of keyhole porosity with increasing VED values was also reported.[20] These relationships can be stated very generically as general applicable tendencies[11] in a parameter optimization process. Therefore, the VED is often seen as a comparison value to support the screening of a process parameter range suitable for an optimization target such as part density or even to derive the recommendation of distinct VED values. As different combinations of parameters can have the same VED but different manufacturing results, the uncritical use of the VED as comparison mean should be avoided, as critically discussed by several authors for different alloy systems.[13, 19–22]

The energy input related parameter optimization using small laboratory specimens neglects potential variations in the thermal conditions during real part manufacturing. Recent studies of Solthani-Tehrani *et al.*[23] and Yavari *et al.*[24] showed directly measured (thermograms) and indirectly measured (melt pool dimensions) significant effects of the part geometry on the thermal history during PBF-LB/M production. The thermal history as the interplay of the local and temporal variations in temperature fields over the entire part production is of utmost importance in PBF-LB/M. It has a strong effect on the resulting part properties and, thereby, on the structural integrity of a PBF-LB/M component.[25] In addition, recent studies[26,27] have shown the influence of ILT on the thermal history of a part with severe heat accumulation at rather short ILT. Geometry and processing induced changes of the thermal history are not considered in the discussed parameter optimization processes. For the use of safety relevant parts, the relationship between small laboratory specimens and real part geometries must be clear.[25] The uncritical use of processing parameters stemming from optimizations at small laboratory specimens regardless of the thermal profile of real manufacturing is negligent. Therefore, the limitations of such small cubes as test coupons are investigated in this study.

MATERIALS AND METHODS

This section briefly summarizes the experimental conditions. They are described in more detail in previous publications of the authors,[12,26–29] as this study aims at concentrating the essential results from different experimental campaigns regarding the question on the limitations of laboratory specimens.

Material, machine, and processing parameters

Spherical, gas atomized powder of stainless steel 316L was used, showing the following particle size distribution: $D_{10} = 18.22\,\mu$m, $D_{50} = 30.50\,\mu$m, and $D_{90} = 55.87\,\mu$m. The specimens were produced on a PBF-LB/M machine of type SLM280HL (SLM Solutions Group AG, Lübeck, Germany) using argon as the shielding gas. The processing was conducted using a bidirectional scanning strategy rotating the scan field by 90° after each layer. No interruption per scan vector was allowed, and the vectors were always parallel to one of the edges of the rectangular cross sections. Three different sets of processing parameters were used, which only vary in the scanning velocity. Therefore, they can be compared in terms of the resulting VED and are named hereafter Low VED (49.12 J mm^{-3} with $v_s = 922$ mm s^{-1}), Basis VED (65.48 J mm^{-3} with $v_s = 700$ mm s^{-1}), and High VED (81.85 J mm^{-3} with $v_s = 560$ mm s^{-1}) parameter set. The other parameters were constant: $P_L = 275$ W, $h_s = 0.12$ mm, $t = 0.05$ mm. The spot size was ~80 μm and the base plate heating 100 °C. In addition, a variation in the ILT was conducted at three specific levels: short (18 s), intermediate (65 s), and long (116 s) ILT. This reproduces conditions of different load factor scenarios.

Specimens' geometry

Figure 3 shows a schematic of the three distinct types of specimens, which differ in their lower 30 mm of built height, characterized by their different cross-sectional areas of connection to the build plate. The manufacturing height was 114.5 mm. The specimens are referred to as small, medium, and full connection types throughout this paper. The cross-sectional changes in the z-direction did not change the ILT, as appropriate dummy parts balanced this by scanning without laser power. At least two specimens per parameter combination (ILT, VED, geometry) were fabricated.

In situ thermographic monitoring and temperature analysis

The specimen production was monitored by mid-wave infrared (MWIR) thermography using an off-axis system equipped with an MWIR camera of Type ImageIR8300 (InfraTech GmbH, Dresden, Germany), sensitive in the range from 2 to 5.7 μm. Due to previously determined apparent emissivity values of 316L

25 October 2023 08:06:05

© Author(s) 2023

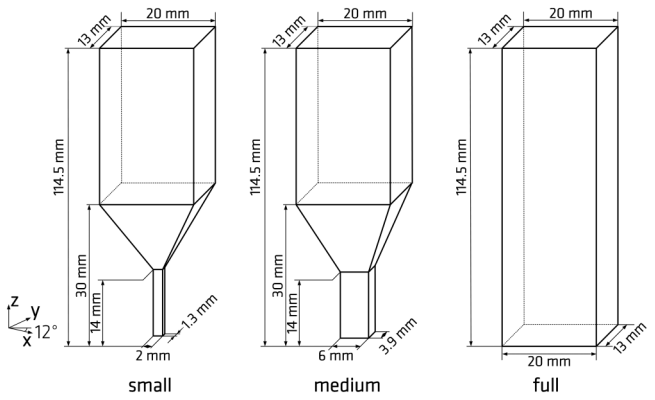

FIG. 3. Schematic of specimens with small, medium, and full connection to the base plate.

powder layers in this setup,[29] the IR intensity signals of the black body calibrated MWIR camera were corrected to true temperature values. The setup was used to acquire layerwise preheating temperatures of the specimens. All analyzed preheating temperatures were acquired from a freshly recoated powder layer. For this, the mean value of a region of interest (ROI) placed in the center of the specimens was considered right before the onset of the next laser exposition. The ROI was of size 11×11 pixels with a pixel length of $\sim 420\,\mu$m. This setup and the specific settings were described in detail in previous work of the authors.[27,29]

Metallography

Metallographic inspection was done at ground and polished cross sections. For porosity analysis, unetched cross sections were taken for optical light microscopy at 20-fold magnification and gray value analysis using the software IMS Client (Imagic Bildverarbeitung AG, Glattbrugg, Switzerland). Melt pool measurements were conducted at the same samples after color etching using Beraha II etching detergent.

RESULTS AND DISCUSSION

The three distinct sets of processing parameters (Low, Basis, and High VEDs), which were used to fabricate the analyzed specimens with different geometries and under different ILT conditions, were chosen based on their ability to produce bulk material with higher density than 99.8% at comparably small build heights (below 12.5 mm).[26] This would have been a typical outcome of a process parameter study using small laboratory specimens. However, the range of different thermal conditions, which may occur during a batch production of a high number of small specimens, is narrow in comparison with real component scenarios: The following presentation of results is an insight into possible variations in the thermal conditions with significant impact on the final part properties using the same processing parameters.[12]

Heat accumulation during the buildup

Variations in the thermal history during production can induce significant differences in the preheating conditions in the course of the layerwise manufacturing process. This can be retraced by the preheating temperature measurements of this study for different experimental levels. Due to interruptions in the experimental IR recordings, the temperature curves are also interrupted and do not cover the entire part production in all cases. Nevertheless, clear general trends are readable from the data. Figure 4 depicts the course of the preheating temperature for the case of full connection type specimens produced by Basis VED at different ILTs.

Three aspects can be directly derived from the diagram: First, heat accumulates in specimens with constant cross section over the build height and can induce significant higher preheating temperatures compared to the initial base plate preheating temperature, which was 100 °C here. Second, this effect is drastically increased when the ILT is reduced. Third, in the case of the batch production of small cubic specimens, such a drastic temperature increase is not expected for two reasons: on the one hand, the build height of density cubes does usually not exceed 15 mm, which corresponds to layer number 300 (in the case of a layer thickness of 50 μm) and, therefore, the accumulation of heat would have not been progressed to high temperatures even in the case of a very short ILT. On the other hand, a typical number of density cubes per build process ranges between 24 and 50. Assuming typical conditions (10 mm edge length of the cubes, a hatch distance of 0.12 mm, a scanning velocity of 725 mm s^{-1}, and a recoating time of 8 s), the ILT of such a build process would range between 42 and 80 s. Therefore, the time for heat dissipation would be long enough to keep the accumulation of heat at a rather low level, comparable to the intermediate ILT curve in Figs. 4 and 5.

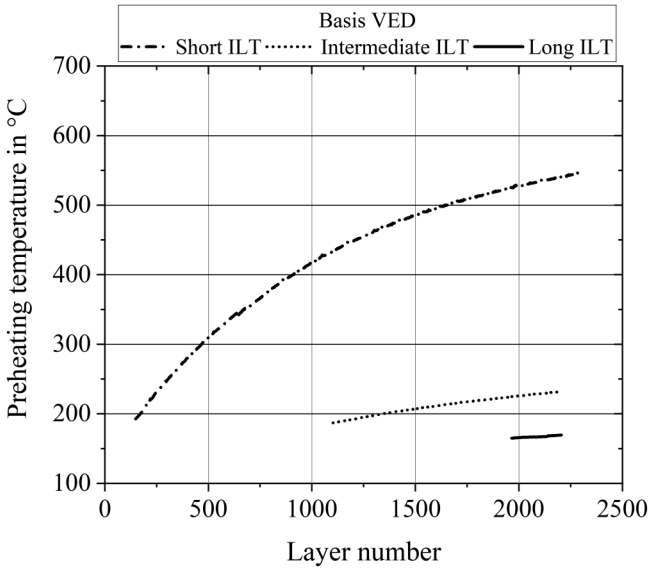

FIG. 4. Preheating temperature over the layer number for Basis VED and full connection type specimens at different ILTs.

25 October 2023 08:06:05

© Author(s) 2023

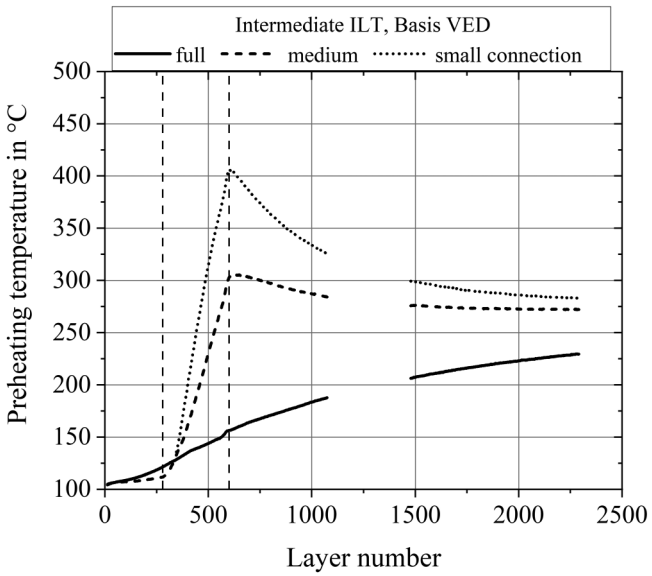

FIG. 5. Preheating temperature over the layer number for Basis VED and intermediate ILT at different connection type specimens. The dotted vertical lines display the start layer and end layer of the frustum.

Figure 5 depicts the course of the preheating temperature for the case of intermediate ILT and Basis VED for the three distinct specimen types. A significant impact of the part geometry on the resulting intrinsic preheating temperatures is revealed. In contrast to the rather constant increase in the preheating temperature over the build height in the case of the full connection type specimen, the course of the preheating temperature is significantly changed by the inverted geometrical frustrum element of the specimens of medium and small connection types. The measured surface temperature increases steeply during the manufacturing of the inverted frustum and reduces again when the cross-sectional constant cuboid volume is produced on top of the necking frustum. Maximum preheating temperatures of up to ~305 and 405 °C were measured.

Kusano and Watanabe[30] have recently presented a thermal history of specimens with similar geometry produced out of Hastelloy X, which was qualitatively in good agreement to the depicted preheating temperature profiles. The geometry of the inverted frustum contributes to the severe heat up, as overhanging structures are prone to accumulation of heat.[31–33] In addition, the necking of the geometry disturbs the heat flux in the z-direction. The contribution of the surrounding powder to heat dissipation via heat conduction is rather limited, as the heat conductivity of the unmolten powder is much smaller than the heat conductivity of the bulk material.[34,35] Gusarov *et al.* appointed a factor of 1/100 as a mean of comparison for the difference in the heat conductivity.[35] Therefore, the predominant share of the heat must dissipate by heat conduction in the z-direction through the bulk material and cannot escape into the powder bed. The reduced cross-sectional areas reduce the heat conduction, while the repeated heat input grows from layer to layer in the overhanging structure, as the cross-sectional areas increase. Consequently, the heat accumulates significantly in that region. The intrinsic preheating temperature declines again in the region of constant cross section and reaches eventually a plateau as the conditions for heat conduction improve in the self-growing heat sink of the cuboid structure. It is important to notice that the highest temperatures were not measured at the highest build height, which contradicts the simplified assumption of a rather constant heating up of build parts in the z-direction. The geometry can significantly impede such a trend. In addition, it is also worth to remind that apart from the geometrical changes, the experimental conditions using Basis VED and intermediate ILT (65 s) could have been also applied for the manufacturing of a batch of small density cubes. However, in density cubes with constant cross sections, such deviations in thermal history are not expected.

So far, the presented results were based on experiments using the Basis VED parameter set. A change in the layerwise energy input by increasing or decreasing the VED through a variation in the scanning velocity does not change the trends of the thermal history qualitatively, but it leads to an elevation or reduction in the preheating temperatures, respectively. This can be exemplarily retraced by Fig. 6, which depicts the course of the preheating temperature of small connection type specimens manufactured at short ILT with the three distinct VED sets. It is worth noticing that the measured preheating temperatures reach maximum temperatures, which are seven times to nine times higher than the base plate preheating temperature. The base plate preheating temperature can be taken as the surface preheating temperature of small density cubes in processing parameter studies.

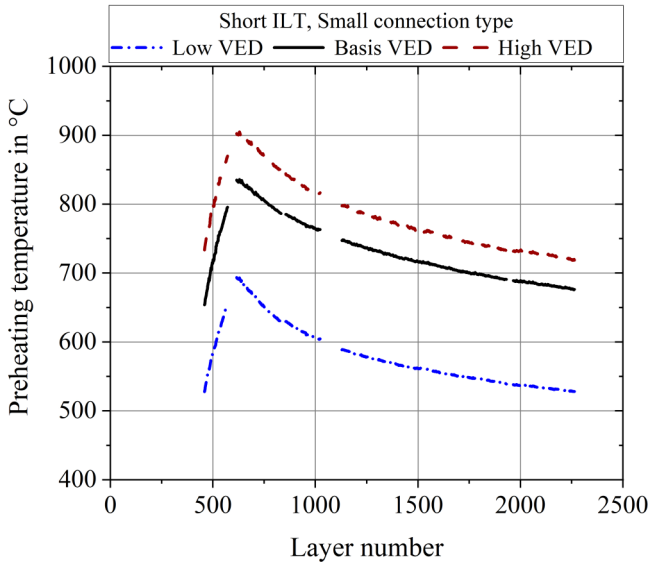

FIG. 6. Preheating temperature over the layer number for a short ILT and small connection type specimens at different VEDs.

25 October 2023 08:06:05

© Author(s) 2023

Effect of ILT on preheating temperature

The discussion of the variability of the thermal history in the production of specimens with distinct boundary conditions (variation in the ILT, geometry, and VED) highlighted the huge effect of the ILT, which was varied on three levels. The results show that there is no simple linear relationship between ILT and resulting heat accumulation in the parts. This becomes clear from Fig. 4, in particular, as the direct comparison of the temperatures of the full connection type specimens produced by Basis VED processing parameters showed rather little difference between intermediate and long ILTs in comparison with the preheating temperatures of the specimen produced with short ILT. To look at this relationship in more detail, the measured preheating temperature of layer 2000 (build height of 100 mm) of the full connection type specimens produced at the three levels of ILT and with three levels of VED is registered in a diagram over the ILT (see Fig. 7). The data points, separated for each VED, can be connected by a function of exponential decay. The determination coefficient R^2 of the curve fitting is high ($R^2 = 0{,}999$) in each case. This relationship can be explained considering the exponential decay of cooling down of a body, which is hotter than its environment according to Newton's law of cooling. The ILT corresponds effectively to the time for heat dissipation before the intake of the next energy input. At longer ILT, more time for the exponential temperature decay is available in every layer and the surface temperature of the specimens is already lower when the next layer is exposed. Conversely, the exposition of layers in case of shorter ILT occurs still at comparably elevated temperatures. This trend accumulates over the course of the production and the ILT contributes exponentially. This means, for constant cross sections, a constant energy input per layer, and a constant ILT per layer, there is an exponential correlation between ILT and the resulting preheating temperature.

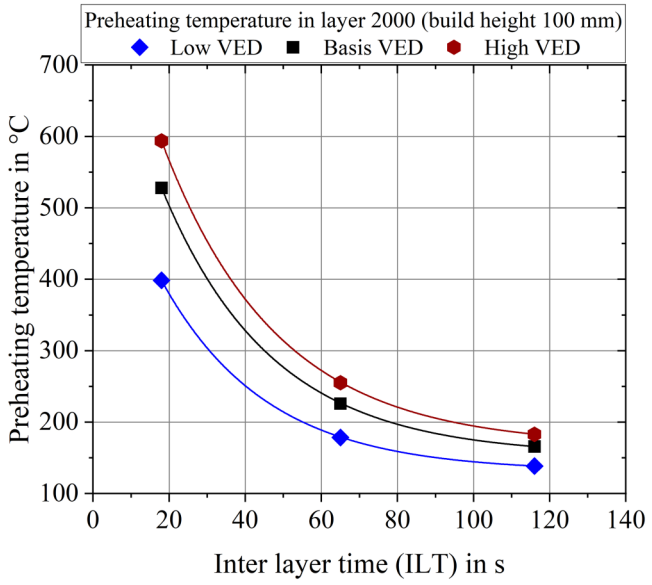

FIG. 7. Preheating temperature in the layer in the case of full connection type specimens in dependence of a constant ILT. The exponential decay curves are fitted.

Variation in melt pool depth

The discussed differences in the thermal history of the specimens, measured by significant variations in the preheating temperature of the parts during production, change the thermal conditions of the laser-material-interaction-zone. An elevation of the preheating temperature by external heating systems is known to increase melt pool sizes.[36,37] Hence, variations in melt pool dimensions can be expected here. Patel and Vlasea[16] defined the stability of a melt pool and its homogenous size distribution over an entire part as a main target for an ideal laser-material-interaction in PBF-LB/M production. Hence, a constant size of the melt pools within a part and in comparison with other parts is a good indicator for a homogenous process result. Melt pool sizes are easy to measure, compared to costly microstructure analysis using electron microscopy. Occurring deviations of the melt pool dimensions can be taken as a starting point for further microstructure analysis. However, there is one drawback of melt pool measurement: due to layerwise remelting, a successful measurement is possible at the last layer only. Therefore, an indirect measurement by correlations with thermal signatures from online monitoring would be desirable. The measured melt pools of the experiments were all identified as melt pools of deep penetration mode welding, according to their aspect ratio (depth:width >1:2[16]). Figure 8 exemplarily illustrates some characteristic shapes of different melt pools of this study.

Figure 9 depicts the melt pool depths measured at a build height of 114.5 mm for the different conditions of the experiments of this study. It also contains the corresponding average preheating temperatures of the top of the specimens (averaged over the last 200 layers). Huge deviations in the melt pool depth can be revealed in dependence on the manufacturing conditions (geometry, ILT, VED). The measured data qualitatively follow the trend of the measured preheating temperature. However, for the individual process parameters, the correlation coefficients between measured melt pool depth and measured preheating temperature seem to differ. This is not surprising, as the effect of the scanning velocity on the melt pool dimensions is known to be stronger than the preheating temperature.[37]

Figure 10 shows the melt pool depths over the preheating temperature separated by the distinct VEDs. Exponential curves are fitted to the experimentally determined measuring data (full dots in the diagram) of the Basis VED ($R^2 = 0.890$, adjusted $R^2 = 0.860$) and High VED ($R^2 = 0.980$, adjusted $R^2 = 0.920$) data with high coefficients of determination. Linear fits for the Basis VED ($R^2 = 0.851$, adjusted $R^2 = 0.826$) and High VED ($R^2 = 0.953$, adjusted $R^2 = 0.938$) showed minor coefficients of determination instead. However, the adjusted R^2 values of the linear fits are close to the values of the exponential fits and, in the case of High VED, even a bit higher. For the data of Low VED, no suitable exponential curve could be fitted, but a linear fit with $R^2 = 0.991$ (adjusted $R^2 = 0.989$) was found. Scipioni Bertoli *et al.*[38] determined the three-dimensional temperature field for an exposition in the

25 October 2023 08:06:05

© Author(s) 2023

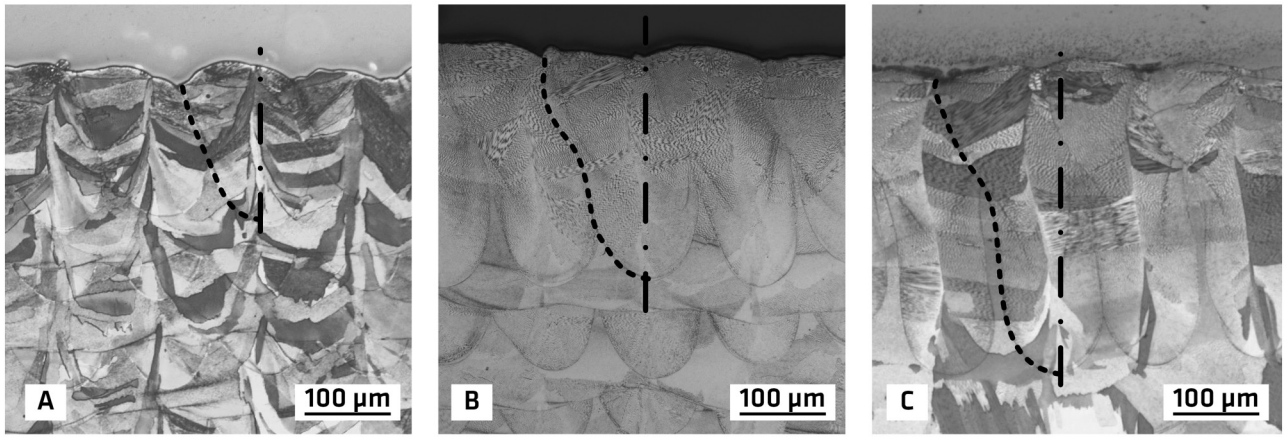

FIG. 8. Etched cross sections with highlighted melt pool boundary of full connection type specimens, build height of 114.5 mm. A: Long ILT, Low VED; B: intermediate ILT, Basis VED; C: short ILT, High VED.

x-direction using Rosenthal's simple analytical approach to the point heat source model by the following equation:

$$T = T_0 + \frac{P_L A}{4\pi\lambda} \cdot \frac{e^{-\frac{v_S(x+r)}{a}}}{r}, \tag{2}$$

with preheating temperature T_0, laser absorption coefficient A, laser power P_L, scanning velocity v_S, thermal diffusivity a, thermal conductivity λ, and the radial distance to the heat source r. An estimation of the melt pool depth was done using Eq. (2) to calculate the radial distance r for the distinct scanning velocities of the study at different preheating temperatures as melt pool depth. For the calculation, liquidus temperature $T_L = 1723$ K,[39] $a = 0.05$ cm^2 s^{-1} (Ref. 38) as thermal diffusivity, $\lambda = 30.08$ W m^{-1} K^{-1} (Ref. 39) as thermal conductivity, and three different absorption coefficients were used (A = 0.8 for High VED, A = 0.6 for Basis VED, A = 0.4 for Low VED). The estimation results are also plotted in Fig. 10. The calculations show a surprisingly good agreement with the estimation results and the measured data. The exponential relationship between preheating temperature and melt pool depth seems to be backed by the Rosenthal model. For the experimentally determined Low VED data, the data volume might have been too small to reveal this relationship.

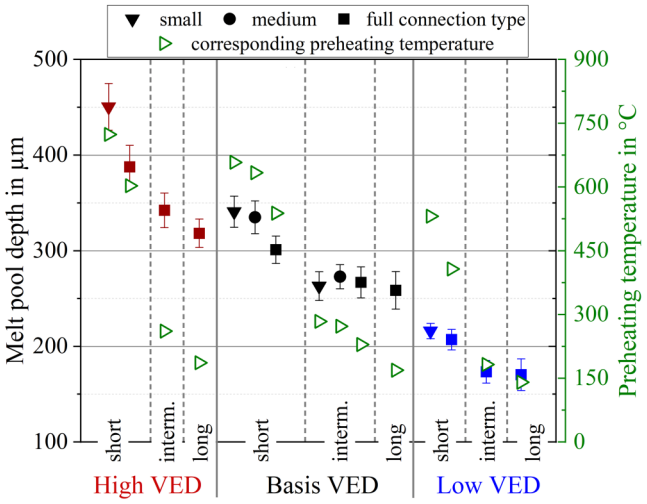

FIG. 9. Melt pool depth and average preheating temperature under several experimental conditions.

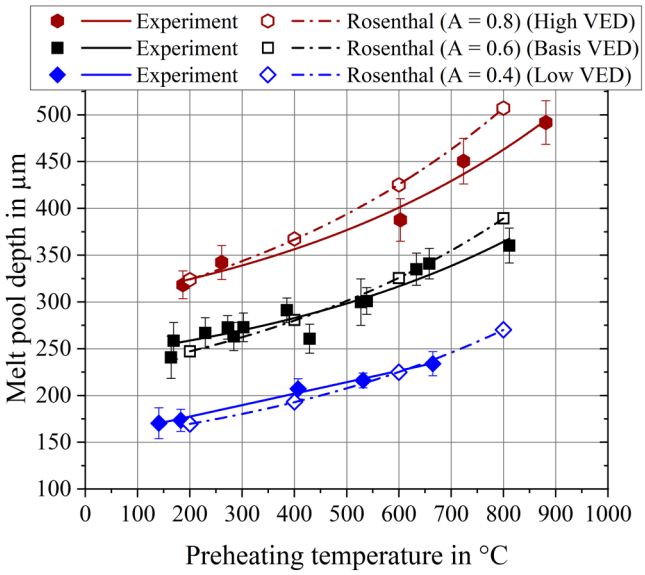

FIG. 10. Melt pool depth over preheating temperature, experimentally measured and estimated by use of Rosenthal's point heat source.

25 October 2023 08:06:05

© Author(s) 2023

The choice of different absorption coefficients for the different VED conditions has been motivated by the work of Trapp *et al.*[40] who measured the absorption coefficients of a 1070 nm cw laser at bare sheets and metal-powder coated disks for 316L and revealed the course of increasing laser absorption during melting mode changes. Interestingly, they determined absorption coefficients between 0.35 and 0.42 in the case of the onset of the transition from conduction mode welding to deep penetration mode welding with non-bimodal melt pool shapes (rather parabolic melt pool shapes, as also described by Cunningham *et al.*[41]). This bimodal melt pool shape (classical keyhole shape) was, in some cases, not significantly and, in other cases, not at all pronounced in the case of Low VED parameters, as can be seen in Fig. 8(a), which shows a rather parabolic melt pool shape. Therefore, it seems reasonable to use an absorption coefficient of 0.4 for the Low VED parameter set. This is also in good agreement with simulative results and its experimental validations by work of Khan *et al.*,[39] when they used a similar processing parameter set. In the case of higher VED but still with the same absorption coefficient, their simulation results underestimated the melt pool depth.[39] Therefore, a higher absorption coefficient was taken for the High VED parameter set of this study. Here, an absorption coefficient of 0.8 was chosen according to Patel and Vlasea,[16] which is also close to the saturation value determined by Trapp *et al.*[40] (0.78). For the Basis VED parameter set, an absorption coefficient of 0.6 works well with this simplified estimation approach, which suggests that the absorption saturation threshold is not reached for the choice of the specific processing parameters. It is worth noting that this simplified calculation of the correlation between preheating temperature and melt pool depth using Rosenthal's point heat source can only be used as a very rough first estimation, as Rosenthal's approach does not consider the deep penetration melt pool shapes. In addition, it neglects any hydrodynamics within the melt. Furthermore, the use of a volumetric heat source model respecting the Gaussian intensity distribution of the real laser beam as well as the consideration of evaporation effects is expected to deliver more precise results at the cost of simplicity.[42]

Notwithstanding the discussed limitations of the presented correlations between preheating temperature and melt pool size, it is revealed by the measurements that the variations in the preheating temperature significantly affect the resulting melt pool dimensions. The preheating temperature variations were triggered by differences in the manufacturing conditions. Hence, inhomogeneities in the melt pool sizes can be expected when significant changes in the thermal conditions occur during real part manufacturing. This indicates already further inhomogeneity of the resulting microstructure, as differences in the thermal gradients during solidification can be expected. However, this thermal issue is not covered by the parameter development in the batch production of small cubic samples.

Shifting of the processing window—Occurring defects

An elevation in the macroscopic part temperature during processing, in particular, an elevation in the preheating temperature of the topmost layers, rises the prevailing energy level in the laser-material-interaction-zone. It effectively changes the initial thermal conditions of the laser melting process. This combined with a constant external energy addition by laser absorption can lead to an overall excessive energy input, which can result in the onset of melt pool instabilities and vapor bubble entrapment by the liquid melt, known as keyhole porosity after complete solidification. The same set of processing parameters, which produces almost fully dense small cubic specimens, might induce keyhole porosity when the thermal preconditions during manufacturing change. Effectively, a change in the thermal preconditions can lead to a critical shift of the processing window determined in a parameter study at small specimens under rather constant thermal conditions. This effect is demonstrated by the results of density measurements at different locations within the specimens. Figure 11 exemplarily

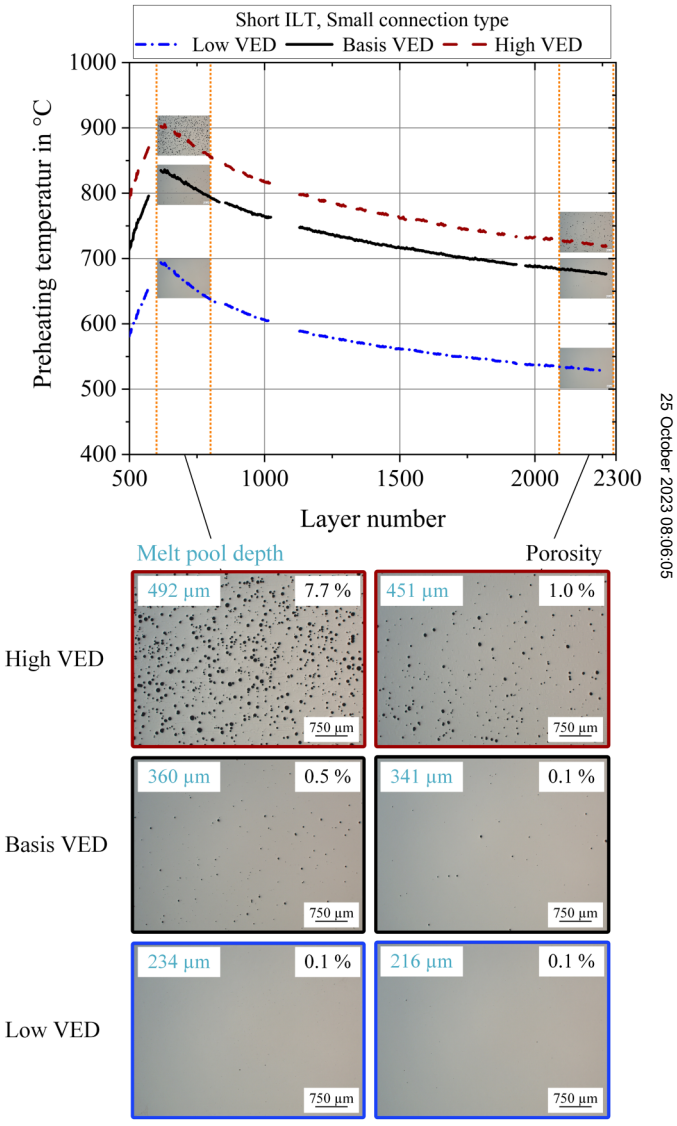

FIG. 11. Porosity increase starts at critical preheating temperatures, which differ for distinct processing parameters.

25 October 2023 08:06:05

© Author(s) 2023

depicts the results of the density measurements at small connection type specimens produced with short ILT. The causality of the elevated preheating temperatures for the shift toward unstable melting conditions, and the resulting keyhole porosity can be directly revealed from the temperature curves and the respective magnification of the unetched cross sections. It is necessary to note that the preheating temperature alone cannot be taken for any result prediction, but the specific processing parameter set must be combinedly considered already discussed for the variation in melt pool sizes.

CONCLUSIONS

PBF-LB/M process parameters, which can be used to produce almost fully dense (density higher than 99.8%) small cubic samples out of 316L, were tested under different processing conditions. Changes in the geometry as well as changes in the interlayer time triggered severe variations in the thermal history, resulting in the significant alteration of the melt pool dimensions and eventually a shift of the process window with occurring keyhole porosity in specific cases. The presented results would not have been revealed by any process parameter optimization using typical 10–15 mm small cubic samples as test coupons. In addition, correlations between the thermographically measured intrinsic preheating temperatures and the resulting melt pool depth were identified. The results underline the importance of the knowledge about the temperature profile during the production of real part geometries. It also stresses the necessity to determine the robustness of specific processing parameters against detrimental process window shifts. The results originating solely from classical density cubes and low temperature processes need to be critically reassessed when significant accumulation of heat occurs during real part manufacturing.

It is, therefore, suggested to determine material specific limitations of tolerable preheating temperatures in the early stage of the processing parameter optimization. Furthermore, the monitoring of the thermal history either by the use of a thermographic measuring equipment or by the use of experimentally validated numerical simulations is recommended to ensure that these predetermined temperature limits are met. In the case of exceeding these limits, an adjustment of the process, e.g., by the integration of additional time for heat dissipation through purposely prolonging the ILT, could be a simple solution without the necessity to manipulate the laser processing parameters itself. The next and more sophisticated step could then be the design of representative test specimens, on which the critical thermal profile of a real part geometry will be transferred.[43] This would enable the evaluation of the properties of the real part geometry without destroying the actual component.

AUTHOR DECLARATIONS

Conflict of Interest

The authors have no conflicts to disclose.

Author Contributions

Gunther Mohr: Conceptualization (equal); Data curation (equal); Formal analysis (equal); Investigation (equal); Methodology (equal); Validation (equal); Visualization (equal); Writing – original draft (equal); Writing – review & editing (equal). **Simon J. Altenburg:** Resources (equal); Writing – review & editing (equal). **Kai Hilgenberg:** Resources (equal); Supervision (equal); Writing – review & editing (equal).

REFERENCES

[1]E. Wycisk, M. Munsch, and M. Schmidt-Lehr, *AMPOWER Report 2021: Additive Manufacturing Market Report* (AMPOWER GmbH & Co. KG, Hamburg, 2021).

[2]T. DebRoy , H. L. Wei, J. S. Zuback, T. Mukherjee, J. W. Elmer, J. O. Milewski, A. M. Beese, A. Wilson-Heid, A. De, and W. Zhang, "Additive manufacturing of metallic components—Process, structure and properties," Prog. Mater. Sci. **92**, 112–224 (2018).

[3]M. Gorelik, "Additive manufacturing in the context of structural integrity," Int. J. Fatigue **94**, 168–177 (2017).

[4]N. Sanaei, A. Fatemi, and N. Phan, "Defect characteristics and analysis of their variability in metal L-PBF additive manufacturing," Mater. Des. **182**, 108091 (2019).

[5]A. Ahmadi, R. Mirzaeifar, N. S. Moghaddam, A. S. Turabi, H. E. Karaca, and M. Elahinia, "Effect of manufacturing parameters on mechanical properties of 316L stainless steel parts fabricated by selective laser melting: A computational framework," Mater. Des. **112**, 328–338 (2016).

[6]G. B. Bang, W. R. Kim, H. K. Kim, H.-K. Park, G. H. Kim, S.-K. Hyun, O. Kwon, and H. G. Kim, "Effect of process parameters for selective laser melting with SUS316L on mechanical and microstructural properties with variation in chemical composition," Mater. Des. **197**, 109221 (2021).

[7]X.-q. Yang, Y. Liu, J.-w. Ye, R.-q. Wang, T.-c. Zhou, and B.-y. Mao, "Enhanced mechanical properties and formability of 316L stainless steel materials 3D-printed using selective laser melting," Int. J. Miner. Metall. Mater. **26**, 1396–1404 (2019).

[8]T. Larimian, M. Kannan, D. Grzesiak, B. AlMangour, and T. Borkar, "Effect of energy density and scanning strategy on densification, microstructure and mechanical properties of 316L stainless steel processed via selective laser melting," Mater. Sci. Eng., A **770**, 138455 (2020).

[9]J. Suryawanshi, K. G. Prashanth, and U. Ramamurty, "Mechanical behavior of selective laser melted 316L stainless steel," Mater. Sci. Eng., A **696**, 113–121 (2017).

[10]A. Röttger, J. Boes, W. Theisen, M. Thiele, C. Esen, A. Edelmann, and R. Hellmann, "Microstructure and mechanical properties of 316L austenitic stainless steel processed by different SLM devices," Int. J. Adv. Manuf. Technol. **108**, 769–783 (2020).

[11]D. Herzog, V. Seyda, E. Wycisk, and C. Emmelmann, "Additive manufacturing of metals," Acta Mater. **117**, 371–392 (2016).

[12]G. Mohr, *Einfluss prozess- und geometrieinduzierter Wärmeakkumulation auf die Werkstoffeigenschaften laserstrahlgeschmolzener metallischer Bauteile* (Fraunhofer Verlag, Stuttgart, Germany, 2022).

[13]G. V. de Leon Nope, L. I. Perez-Andrade, J. Corona-Castuera, D. G. Espinosa-Arbelaez, J. Muñoz-Saldaña, and J. M. Alvarado-Orozco, "Study of volumetric energy density limitations on the IN718 mesostructure and microstructure in laser powder bed fusion process," J. Manuf. Process. **64**, 1261–1272 (2021).

[14]A. Carrozza, A. Aversa, P. Fino, and M. Lombardi, "A study on the microstructure and mechanical properties of the Ti-6Al-2Sn-4Zr-6Mo alloy produced via laser powder bed fusion," J. Alloys Compd. **870**, 159329 (2021).

[15]Y. M. Wang, C. Kamath, T. Voisin, and Z. Li, "A processing diagram for high-density Ti-6Al-4V by selective laser melting," Rapid Prototyp. J. **24**, 1469–1478 (2018).

[16]S. Patel and M. Vlasea, "Melting modes in laser powder bed fusion," Materialia **9**, 100591 (2020).

[17]C. Britt, C. J. Montgomery, M. J. Brand, Z.-K. Liu, J. S. Carpenter, and A. M. Beese, "Effect of processing parameters and strut dimensions on the

25 October 2023 08:06:05

© Author(s) 2023

microstructures and hardness of stainless steel 316L lattice-emulating structures made by powder bed fusion," Addit. Manuf. **40**, 101943 (2021).
[18]A. M. Rubenchik, W. E. King, and S. S. Wu, "Scaling laws for the additive manufacturing," J. Mater. Process. Technol. **257**, 234–243 (2018).
[19]U. Scipioni Bertoli, A. J. Wolfer, M. J. Matthews, J.-P. R. Delplanque, and J. M. Schoenung, "On the limitations of volumetric energy density as a design parameter for selective laser melting," Mater. Des. **113**, 331–340 (2017).
[20]M. Giovagnoli, G. Silvi, M. Merlin, and M. T. Di Giovanni, "Optimisation of process parameters for an additively manufactured AlSi10Mg alloy: Limitations of the energy density-based approach on porosity and mechanical properties estimation," Mater. Sci. Eng., A **802**, 140613 (2021).
[21]K. G. Prashanth, S. Scudino, T. Maity, J. Das, and J. Eckert, "Is the energy density a reliable parameter for materials synthesis by selective laser melting?," Mater. Res. Lett. **5**, 386–390 (2017).
[22]R. Zhao, C. Chen, W. Wang, T. Cao, S. Shuai, S. Xu, T. Hu, H. Liao, J. Wang, and Z. Ren, "On the role of volumetric energy density in the microstructure and mechanical properties of laser powder bed fusion Ti-6Al-4 V alloy," Addit. Manuf. **51**, 102605 (2022).
[23]A. Soltani-Tehrani, R. Shrestha, N. Phan, M. Seifi, and N. Shamsaei, "Establishing specimen property to part performance relationships for laser beam powder bed fusion additive manufacturing," Int. J. Fatigue **151**, 106384 (2021).
[24]M. Yavari, R. Williams, A. Riensche, P. A. Hooper, K. D. Cole, L. Jacquemetton, H. S. Halliday, and P. Rao, "Thermal modeling in metal additive manufacturing using graph theory-application to laser powder bed fusion of a large volume impeller," Addit. Manuf. **41**, 101956 (2021).
[25]R. Shrestha, N. Shamsaei, M. Seifi, and N. Phan, "An investigation into specimen property to part performance relationships for laser beam powder bed fusion additive manufacturing," Addit. Manuf. **29**, 100807 (2019).
[26]G. Mohr, S. J. Altenburg, and K. Hilgenberg, "Effects of inter layer time and build height on resulting properties of 316L stainless steel processed by laser powder bed fusion," Addit. Manuf. **32**, 101080 (2020).
[27]G. Mohr, K. Sommer, T. Knobloch, S. J. Altenburg, S. Recknagel, D. Bettge, and K. Hilgenberg, "Process induced preheating in laser powder bed fusion monitored by thermography and its influence on the microstructure of 316L stainless steel parts," Metals **11**, 1063 (2021).
[28]G. Mohr, N. Scheuschner, and K. Hilgenberg, "In situ heat accumulation by geometrical features obstructing heat flux and by reduced inter layer times in laser powder bed fusion of AISI 316L stainless steel," Proc. CIRP **94**, 155–160 (2020).
[29]G. Mohr, S. Nowakowski, S. J. Altenburg, C. Maierhofer, and K. Hilgenberg, "Experimental determination of the emissivity of powder layers and bulk material in laser powder bed fusion using infrared thermography and thermocouples," Metals **10**, 1546–1557 (2020).
[30]M. Kusano and M. Watanabe, "Microstructure control of Hastelloy X by geometry-induced elevation of sample temperature during a laser powder bed fusion process," Mater. Des. **222**, 111016 (2022).
[31]Q. Han, H. Gu, S. Soe, R. Setchi, F. Lacan, and J. Hill, "Manufacturability of AlSi10Mg overhang structures fabricated by laser powder bed fusion," Mater. Des. **160**, 1080–1095 (2018).
[32]A. Ilin, R. Logvinov, A. Kulikov, A. Prihodovsky, H. Xu, V. Ploshikhin, B. Günther, and F. Bechmann, "Computer aided optimisation of the thermal management during laser beam melting process," Phys. Procedia **56**, 390–399 (2014).
[33]O. Illies, G. Li, J.-P. Jürgens, V. Ploshikhin, D. Herzog, and C. Emmelmann, "Numerical modelling and experimental validation of thermal history of titanium alloys in laser beam melting," Proc. CIRP **74**, 92–96 (2018).
[34]L. C. Wei, L. E. Ehrlich, M. J. Powell-Palm, C. Montgomery, J. Beuth, and J. A. Malen, "Thermal conductivity of metal powders for powder bed additive manufacturing," Addit. Manuf. **21**, 201–208 (2018).
[35]A. Gusarov, I. Yadroitsev, P. Bertrand, and I. Smurov, "Model of radiation and heat transfer in laser-powder interaction zone at selective laser melting," J. Heat Transfer **131**, 072101 (2009).
[36]I. Yadroitsev, P. Krakhmalev, I. Yadroitsava, S. Johansson, and I. Smurov, "Energy input effect on morphology and microstructure of selective laser melting single track from metallic powder," J. Mater. Process. Technol. **213**, 606–613 (2013).
[37]A. Vasinonta, J. L. Beuth, and M. Griffith, "Process maps for predicting residual stress and melt pool size in the laser-based fabrication of thin-walled structures," J. Manuf. Sci. Eng. **129**, 101–109 (2007).
[38]U. Scipioni Bertoli, B. E. MacDonald, and J. M. Schoenung, "Stability of cellular microstructure in laser powder bed fusion of 316L stainless steel," Mater. Sci. Eng., A **739**, 109–117 (2019).
[39]K. Khan, G. Mohr, K. Hilgenberg, and A. De, "Probing a novel heat source model and adaptive remeshing technique to simulate laser powder bed fusion with experimental validation," Comput. Mater. Sci. **181**, 109752 (2020).
[40]J. Trapp, A. M. Rubenchik, G. Guss, and M. J. Matthews, "In situ absorptivity measurements of metallic powders during laser powder-bed fusion additive manufacturing," Appl. Mater. Today **9**, 341–349 (2017).
[41]R. Cunningham, C. Zhao, N. Parab, C. Kantzos, J. Pauza, K. Fezzaa, T. Sun, and A. D. Rollett, "Keyhole threshold and morphology in laser melting revealed by ultrahigh-speed x-ray imaging," Science **363**, 849–852 (2019).
[42]A. Artinov, M. Bachmann, and M. Rethmeier, "Equivalent heat source approach in a 3D transient heat transfer simulation of full-penetration high power laser beam welding of thick metal plates," Int. J. Heat Mass Transfer **122**, 1003–1013 (2018).
[43]U. Zerbst, G. Bruno, J.-Y. Buffiere, T. Wegener, T. Niendorf, T. Wu, X. Zhang, N. Kashaev, G. Meneghetti, N. Hrabe, M. Madia, T. Werner, K. Hilgenberg, M. Koukolíková, R. Procházka, J. Džugan, B. Möller, S. Beretta, A. Evans, R. Wagener, and K. Schnabel, "Damage tolerant design of additively manufactured metallic components subjected to cyclic loading: State of the art and challenges," Prog. Mater. Sci. **121**, 100786 (2021).

25 October 2023 08:06:05

© Author(s) 2023